Neural Networks for Medical Data Processing: Segmentation of Fluorescence Lifetime Imaging Microscopy

Ilya Shchechkin[1,2*], Svetlana Rodimova[1], Artem Mozherov[3], Vadim Elagin[1], Nikolai Bobrov[4], Vladislav Shcheslavsky[1], Vladimir Zagainov[4,5], Elena Zagaynova[1,6], and Daria Kuznetsova[1,3]

[1] Privolzhsky Research Medical University, Institute of Experimental Oncology and Biomedical Technologies, 10/1 Minin and Pozharsky sq., Nizhny Novgorod 603950, Russian Federation

[2] N.I. Lobachevsky Nizhny Novgorod National Research State University, 23 Gagarina ave., Nizhny Novgorod 603022, Russian Federation

[3] I.M. Sechenov First Moscow State Medical University, Moscow 119991, Russian Federation

[4] The Volga District Medical Centre of Federal Medical and Biological Agency, 14 Ilinskaya str., Nizhny Novgorod 603000, Russian Federation

[5] Nizhny Novgorod Regional Clinical Oncologic Dispensary, 11/1 Delovaya str., Nizhny Novgorod 603126, Russian Federation

[6] Lopukhin Federal Research and Clinical Center of Physical-Chemical Medicine of Federal Medical Bio-logical Agency, 1a Malaya Pirogovskaya str., Moscow 119435, Russian Federation

*e-mail: Iliahasa1992@gmail.com

Abstract. Fluorescence lifetime imaging microscopy (FLIM) is a powerful tool for visualizing the distribution of fluorescence lifetimes of fluorophores within a tissue, and is used for optical metabolic imaging. However, processing the large volumes of data generated by FLIM can be time-consuming and challenging for an untrained operator. Convolutional neural networks (CNNs) have demonstrated its effectiveness for tissue image and FLIM segmentation, making them a promising tool for automated analysis of FLIM images. The article presents a method for segmenting FLIM images of liver tissue during the regeneration using a CNN based on the UNet++ architecture. The CNN was trained to detect cell boundaries and nuclei, and the resulting masks were used to approximate the fluorescence decay curves for the FLIM-image data. The results show that the CNN is effective in segmenting FLIM images of cells and tissues, and obtaining fluorescence decay curves. The use of CNNs and other machine learning methods in medical image segmentation and analysis will improve and speed up diagnosis and reduce diagnostic errors.

Keywords: deep learning; segmentation; convolutional neural networks; FLIM; liver regeneration; multiphoton microscopy.

Paper #9278 received 30 May 2025; revised manuscript received 22 Jul 2025; accepted for publication 2 Aug 2025; published online 21 Sep 2025. doi: 10.18287/JBPE25.11.030304.

1 Introduction

Fluorescence lifetime imaging microscopy (FLIM) is a powerful tool for visualization of the distribution of fluorescence lifetimes of fluorophores within a tissue. It enables researchers not only to differentiate fluorophores, but also, more importantly, to probe their environment, since the fluorescence lifetime of a fluorophore depends on the pH, viscosity, temperature and other physicochemical parameters of the region of the medium in which it is located. One of the most important applications of FLIM is for optical metabolic imaging. This is based on measurements of the decay kinetics of endogenous fluorophores such as NAD(P)H and FAD, which participate in redox reactions in a cell and, accordingly, reflect its metabolic status [1].

To describe the decay of NAD(P)H fluorescence, bi-exponential or tri-exponential approximation models are usually used, where the parameters t_1, t_2 and t_3 correspond to the lifetimes of the free, bound and phosphorylated forms of NAD(P)H, respectively, and their contributions are described by the relative amplitudes a_1, a_2 and a_3. Changes in the NAD(P)H fluorescence decay curves can therefore serve to indicate metabolic changes: while an increase in a_1 correlates with an increase in anaerobic glycolysis, an increase in a_2 is associated with an increase in oxidative phosphorylation, and a change in a_3 corresponds to changes in the intensity of the synthetic processes in the cells. FLIM generates a large amount of information – the times of registration of photons, their number, as well as data on the coordinates of where the photons are recorded. Processing such large volumes of data can be time-consuming and challenging for an untrained operator.

Neural networks are increasingly being used in medical data analysis due to their ability to learn complex patterns and relationships in large data sets. In particular, convolutional neural networks (CNNs) have demonstrated significant success in tissue image and FLIM segmentation [2, 3].

A CNN is a type of deep learning algorithm that can automatically learn features from images and classify them into different categories. This type of algorithm is particularly well suited to image segmentation problems, where the goal is to divide an image into different regions based on their contents. CNNs have previously been shown to be effective in segmenting liver tissue as seen in multiphase CT images [4].

Liver tissue segmentation is an important task in medical imaging because it enables the detection and diagnosis of early metabolic changes associated with liver diseases such as hepatocellular carcinoma (HCC) [4]. Traditional tissue segmentation methods rely on manual annotation, which is time-consuming and prone to human error. FLIM, on the other hand, produces large data sets that may contain ambiguous objects to assess, which can make processing difficult for the operator.

A promising task is to develop an algorithm for automatic image analysis of FLIM microscopy to improve the clinical diagnosis of metabolic changes in tissues in the analysis of various conditions, disease development, tumor growth, and treatment response. In the case of scientific research, in turn, the development of a method for analyzing large amounts of data is required, which can be solved by developing automated algorithms.

The objective of the work is to develop an algorithm for automated analysis of FLIM images for subsequent software development.

FLIM image analysis using neural networks can be performed in various ways. Using neural networks to calculate the fluorescence decay parameters for all pixels in an image, or by segmenting and then calculating the decay parameters either based on an approximation, in SPCImage, or based on the results of parameter calculations using neural networks, or by approximating the decay curves using a separate curve approximator. In this paper, we consider the development of an algorithm for analyzing FLIM images of liver tissue during regeneration against the background of pathology, based on the previously presented in Ref. [5]. CNN-based automated FLIM analysis methods have been applied for the first time to a complex *in vivo* model.

2 Materials and Methods

2.1 FLIM Data Processing

To study the possibility of employing automated analysis of FLIM images using CNN, it was decided to analyze the effectiveness of automatic processing of images obtained from FLIM data arrays for various study samples derived with this method.

Models of liver regeneration with pathologies (fibrosis and steatosis) were selected as such samples.

Data from the studied samples had previously been processed manually and had also had metabolic changes confirmed on the basis of other methods (histology, molecular analysis) [6]. From comparisons with the manually processed data, conclusions were drawn regarding the feasibility of such automated processing.

Since specific fluorescence parameters obtained from manual and automatic processing may differ markedly from each other due to limitations of fitting, it was decided to compare the ability to detect identical patterns of changes in metabolic status at different time points, rather than to use absolute values, for the variants of manual and automatic processing. The coincidence of global changes in metabolic parameters (relative contributions to the mean time) was thus considered as a sign of the effectiveness of the automatic analysis.

The criterion for change in the metabolic status of each studied object was taken as any significant difference between the fluorescence lifetime parameters (t_1, t_2, t_3, a_1, a_2, a_3) at different time points of the study.

FLIM images were labeled (segmented) using ImageJ (Fiji) into three classes, class 1 representing the cell boundary, class 2 the nucleus boundary, class 0 everything else. To train a CNN to detect the cells, three mask variants were used: cell borders, complete cells, background without cells.

To carry out automated analysis, a convolutional neural network was trained, for which the UNet++ architecture was chosen that used a multi-component loss function consisting of the BCE, Focal and Dice functions. The CNN was trained in a three-channel format, receiving all previously designated mask options as its input. The following quality metrics were used: area under the curve (AUC) and the F_1-metric.

A separate CNN was also trained to identify cell nuclei and subsequently to exclude them from the analysis. BCE was used as the loss function; the area under the curve (AUC) and F_1-metric were used as quality metrics.

The images were additionally filtered by brightness to exclude bright areas (vitamin A and lipofuscin) from the analysis. Using the Otsu method with two thresholds, its own thresholds were automatically selected for each image, since there is a difference in intensity among the images.

The resulting predictions were used for cell-by-cell segmentation of the corresponding images. The segmentation results were then used as fields to perform cell-by-cell analysis of the fluorescence decay of each image using an exponentially modified Gaussian function, effectively describing bi-exponential and tri-exponential decay models. For each cell, the coefficients of the fluorescence decay curve equation were calculated, on the basis of which the fluorescence lifetime parameters could be determined.

Visual Studio Code (Microsoft, Washington, U.S.) was used as the analysis environment; Python (Python Software Foundation, Delaware, U.S.) was used as the programming language.

2.2 Model of Liver Regeneration

Wistar rats (28 individuals) were used as model objects. To model pathologies, two options were chosen: fibrosis was induced by intraperitoneal injection of a 30% oil solution of CCl4; steatosis was induced by a high-calorie fatty diet, 60% fat in the total diet of the animal. Induction of liver regeneration was initiated by 70% partial hepatectomy, followed by monitoring the regeneration process on days 3 or 7 after hepatectomy, with FLIM imaging at both stages.

To train the CNN, 330 FLIM images of rat liver tissue at various stages of regeneration were used.

The animals were kept before and after the operation in accordance with the rules adopted by the European Convention for the Protection of Vertebrate Animals; and according to the National Institutes of Health Guide for the Care and Use of Laboratory Animals (NIH Publications no. 8023, revised 1978) and also in compliance with the ARRIVE guidelines. The local ethics committee at the Privolzhsky Research Medical University (protocol №15; date: 23.09.2022) approved all the animal procedures.

2.3 CNN Training

A convolutional neural network model was selected for cell-by-cell image segmentation. Threshold segmentation methods are not suitable for this model due to the high intensity heterogeneity, which is associated with the presence of different objects within the same intensity boundaries. Two architectures, UNet and UNet++, were selected as possible options for segmentation [6]. The UNet architecture is a standard variant of biomedical image segmentation due to its high accuracy and ease of implementation, in turn, its modification UNet++, according to literary sources, is one of the most accurate segmenters for biomedical images, although it has a large volume of parameters and training time [7]. Unlike monolithic transformers or context-focused models, like DeepLab, which is better for natural images or ResUNet better for volumetric data, UNet++ offers adaptive precision-speed control and seamless extensibility.

ReLU and ELU were considered as activation functions. BCE, Focal, and Dice were considered as error functions. Various combinations of these options were tested. Training was conducted over 1000 epochs in 10 steps. The F_1 score (Dice metric) was used to evaluate the quality of segmentation.

The UNet++ model, which uses ELU as an activation function and a multicomponent error function, was found to be more computationally complex than the UNet model with ReLU and the BCE error function. As a result, the size of the UNet++ model increased by a factor of 3, from about 35 Mbits for UNet to about 100 Mbits for UNet++. Similarly, the training time for the UNet++ model also increased significantly.

Comparison of architectures is presented in Table 1.

Table 1 Comparison of accuracy of different combinations of segmentation techniques.

Architecture	Activation function	Loss function	F_1-metric
UNet	ReLU	BCE	0.619
UNet++	ReLU	BCE	0.637
UNet++	ELU	BCE	0.649
UNet++	ELU	BCE+Focal	0.664
UNet++	ELU	BCE+Dice	0.671
UNet++	ELU	Dice+Focal	0.689
UNet++	ELU	BCE+Focal+Dice	0.703

Images for CNN training were augmented; areas containing the objects under study were selected from the images, after which the areas were cropped and re-reflected. In this way, a higher resolution image was obtained, individual sections of which were used as different images to increase the volume of training material and the density of objects in the image. Thus, 988 images were accumulated.

The collected images were divided into training and validation sets. The training set was assigned 70% of the images, while the validation set received 30%. Previously accumulated images of normal liver tissue samples were used as a test set.

These images, with applying standard image augmentation techniques (height and width shift, reflection, rotation, horizontal and vertical flip, zoom), were used to train a convolutional neural network based on the UNet++ architecture using a multi-component loss function.

The UNet++ architecture is an encoder-decoder network that nests smaller-depth encoder-decoder layers to reduce the semantic gap between the encoder and decoder feature maps.

Hyperparameters were selected for neural network training. Adam was used as an optimization algorithm

with a learning rate of 0.0001. Due to the limited amount of memory, the batch size was set to 10. Dropuot was used as a regularization method. Early stopping of learning was not used. As a loss function, used to control the quality of model training, a multicomponent function was used; it is a sum of BCE, Focal and Dice loss functions.

The BCE loss function calculates the binary cross entropy, compares the predicted result for each pixel with the real value of 0 or 1, and then calculates a score that penalizes differences between the real and predicted values.

The Focal loss function is a modified version of the BCE function for use in cases with extreme class imbalance.

The Dice loss function is based on calculating the overlap between the predicted and true classes.

The result of using UNet++ is a semantic segmentation map, which should be divided into different objects of the same class using the instance segmentation method.

The classic 'watershed' algorithm was used as an instance segmentation method; this algorithm works by filling a space with known boundaries (cell edge segmentation mask) based on individual markers (whole cell segmentation mask), until the moment of overlapping, at which division into segments occurs. The parameters used by the algorithm (markers of objects, distance between objects) were selected automatically. No significant over- or under-segmentation was detected during image analysis. If there were too small objects on the masks, they were deleted.

The CNN for determining cell boundaries was trained for 1000 epochs, of 10 steps each; the multi-component loss coefficient was 0.6; Focal Loss was 0.075; Dice Loss was 0.22, with an F_1 (Dice) metric of 0.7 (precision was equaled to 0.64 and recall was 0.8), IoU of 0.51, accuracy of 0.76 and AUC of 0.9.

The CNN for kernel detection was trained for 1000 epochs; the F_1 (Dice) metric was 0.65 (precision was equaled to 0.36 and recall was 0.96), IoU of 0.4, accuracy of 0.96 and AUC of 0.98.

The relatively low accuracy of the segmenter is associated with the identification of previously unmarked objects, which was confirmed during manual image verification.

In the case of nuclear detection, a large number of false positive results indicate the detection of rounded low-intensity objects, these may be the lipid droplets or tissue damage. Segmented nuclei or similar objects are removed from the analysis, regardless of whether they are nuclei or other objects of no interest.

In this way, high-accuracy models were trained.

2.4 Segmentation

Using the watershed algorithm, the resulting masks were segmented to obtain individual cell masks for the image. Next, a combined mask was obtained for each cell, including only the cytoplasm of cells of a certain brightness and excluding the nuclei and areas of vitamin A (or lipofuscin) of increased brightness.

The masks were then used as ROIs to approximate the fluorescence decay curves for the FLIM-image data corresponding to this mask, based on an exponentially modified Gaussian function.

For steatosis, 11367 individual decay curves were obtained.

For fibrosis, 9607 individual decay curves were obtained.

Manual processing of this volume of images resulted in 5370 and 3138 decay curves for the steatosis and fibrosis variants, respectively.

2.5 Curve Fitting

The approximation of the curves to calculate the fluorescence decay parameters was carried out based on an exponentially modified Gaussian function, the equivalent form of which is suitable for describing the decay of exponentials:

$$f(x;h;\mu;\sigma;\tau) = \frac{h\sigma}{\tau}\sqrt{\frac{\pi}{2}}exp\left(\frac{1}{2}\left(\frac{\sigma}{\tau}\right)^2 - \frac{x-\mu}{\tau}\right)\times \\ \times erfc\left(\frac{1}{\sqrt{2}}\left(\frac{\sigma}{\tau} - \frac{x-\mu}{\tau}\right)\right).$$

where h – Gaussian amplitude; μ – mean Gaussian value; σ – Gaussian standard deviation; λ – exponent values; τ – relaxation time of the exponent, which is calculated:

$$\tau = \frac{1}{\lambda},$$

and *erfc* is a complete function error:

$$erfc(x) = 1 - erf(x) = \frac{2}{\sqrt{\pi}}\int_x^\infty e^{-t^2}dt.$$

The FLIM parameters were calculated on the basis of the values: h, and λ obtained during the approximation, based on the functions:

$$t_n = \frac{1}{\lambda_n} = \tau_n,$$

$$a_n^{absolute} = \frac{h_n}{t_n},$$

$$a_n^{relative} = \frac{100*a_n^{absolute}}{\sum a_n^{absolute}},$$

$$t_{mean} = \sum a_n \cdot t_n.$$

The initial parameters of the approximation model corresponded to the values obtained for normal liver tissue during manual processing. The a_1, a_2, and a_3 parameters were 60%, 30%, and 10%, respectively, while the t_1, t_2, and t_3 parameters were 0.4, 2.5, and 6 ns, respectively. The parameters were limited to a 50% range of the set value.

The chi-squared metric was used as a metric of approximation accuracy, with the maximum possible threshold value of 1.5.

2.6 Image Processing

Examples of FLIM images are presented in Fig. 1. The stages of operation of the segmenter are also presented in Fig. 1.

When studying metabolic changes in tissues using the FLIM method, three forms of NAD(P)H are used: the free, bound and phosphorylated forms. These are represented by the following decay parameters: their relative contributions to the total decay time a_1, a_2, and a_3 and their absolute values of decay time t_1, t_2, and t_3, respectively. These parameters are calculated by approximating each decay curve based on an exponential Gaussian function for the 3 components. In this case, the parameter $a_3(t_3)$ actually makes only a very small contribution to the approximation of the function, but at the same time it can change the distribution of the two remaining parameters. Therefore, this parameter is an important marker of changes in metabolic status, as it is associated with the phosphorylated form of NADPH, which is involved in the synthetic function of the tissue [7]. Thus, it is important to perform FLIM decay parameter distribution analysis for both the two-component and three-component automatic analysis options (Fig. 2).

It was shown that the decay tails differ for 2 and 3 component approximation variants. The images show that the tail for the three-component approximation fits the data better, although not significantly (Fig. 2).

As a result of the analysis, it was shown that the parameter values for options with two and three components at time points: 0, 3, 6, 9, and 12 weeks of steatosis development, for parameters a_1 and a_2 are similar, which indicates a weak influence of the use of parameter $a_3(t_3)$ on the result of the analysis of the remaining components, which in turn allows the use of a three-component analysis option in the future without loss of accuracy (Fig. 3A, Fig. 4B).

Using the average results of the metabolic parameters for each image is a more representative option for analysis due to the significant leveling of outliers and, in some cases, a reduction of the scatters, but the option of cell-by-cell analysis is more representative of the entire sample (Fig. 3B, Fig.4B).

The results of the analysis are presented in Figs. 2 and 3, Table SI and Table SII.

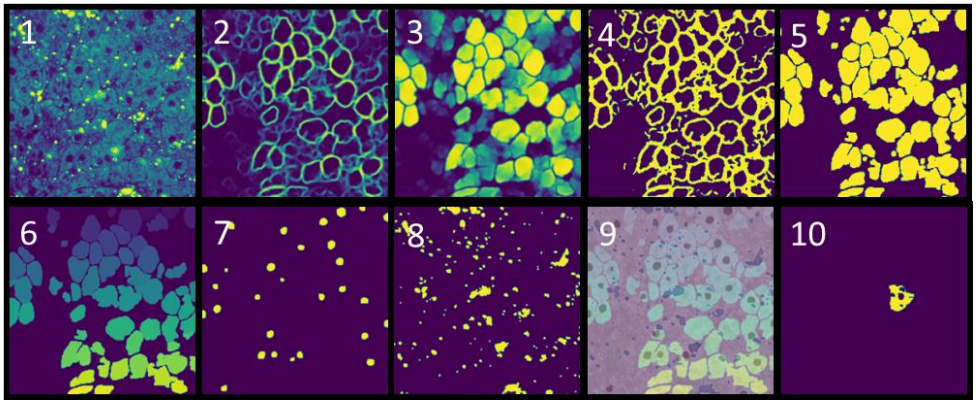

Fig. 1 Stages of image processing to obtain cell masks: 1 – FLIM image; 2 – detected cell boundaries; 3 – detected cells; 4 – boundaries selected relative to the threshold; 5 – cells selected relative to the threshold; 6 – processed cells separated by the watershed algorithm; 7 – detected cell nuclei; 8 – bright areas of inclusions in the image; 9 – joint mask for the image; 10 – mask for one cell, excluding nucleus and bright inclusions.

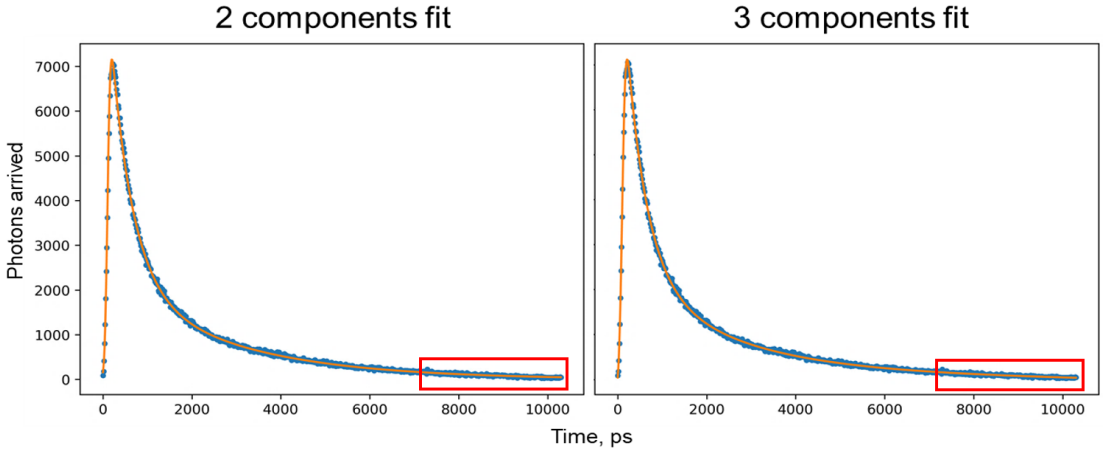

Fig. 2 Results of automatically fitting procedure for 2 and 3 components fitting, for the same sample: blue dots − real fluorescence decay data; orange curve − curve of the approximation function of real data; red box − tail part of the function, for the position of which the third component is responsible.

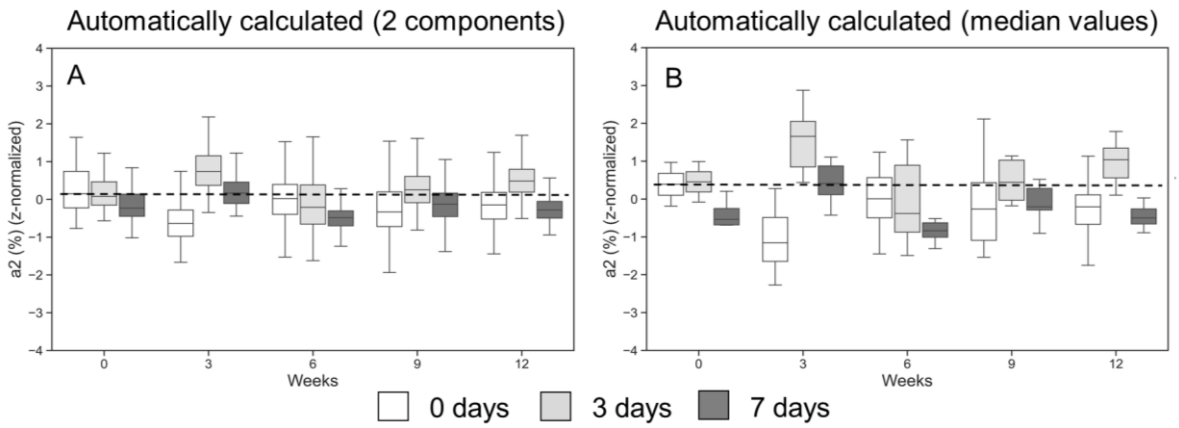

Fig. 3 Graphs of z-normalized values of parameter a_2 for fluorescence decay for (A) automatically calculated steatosis with 2 components fitting, (B) automatically calculated steatosis with median values for each image analyzed. The dotted line is the median of the data for 0 days and 0 weeks.

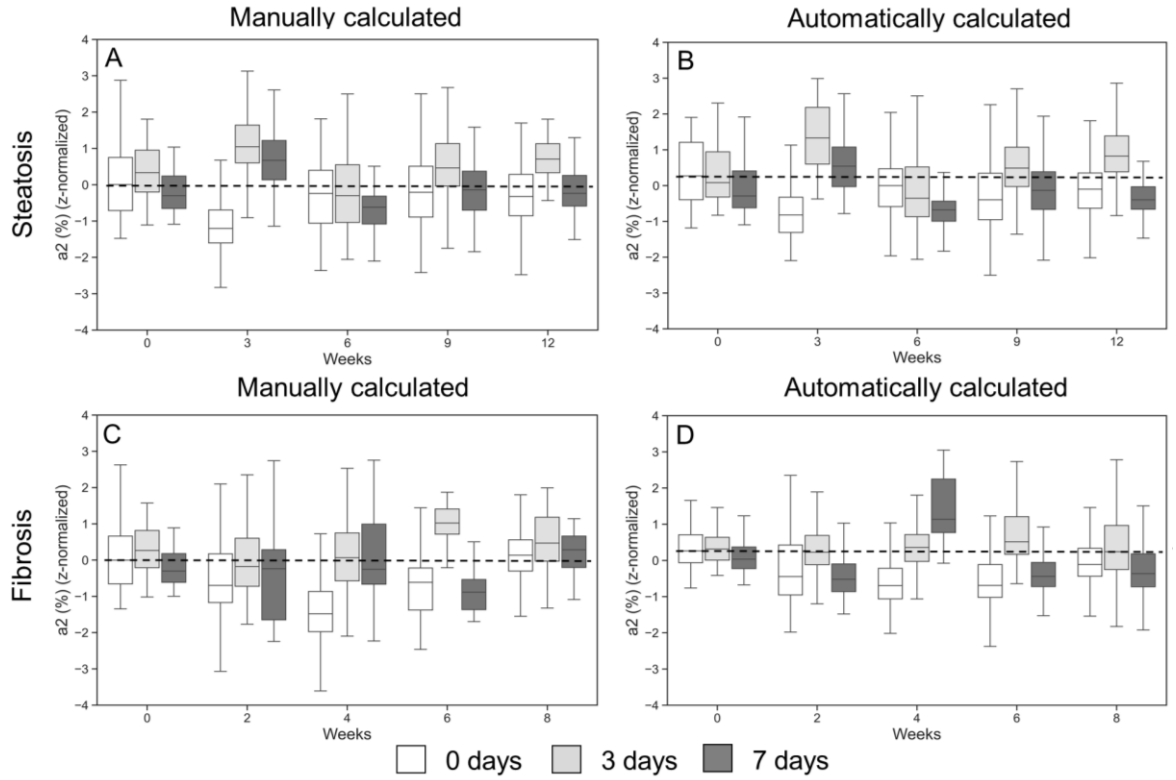

Fig. 4 Graphs of z-normalized values of parameter a_2 for fluorescence decay for different models of metabolic shift, calculated manually or automatically: (A) Manually calculated steatosis, (B) Automatically calculated steatosis, (C) Manually calculated fibrosis, (D) Automatically calculated fibrosis. The dotted line is the median of the data for 0 days and 0 weeks.

3 Results

Our assessment of the possibility of using the automatic method for analyzing FLIM images was carried out using data cell-by-cell, for the automatic version, and by field, for the manual analysis version; the fields conditionally correspond to cells, although they covered 10–20% of the cytoplasm.

When processing steatosis data, the dispersion (Q3–Q1, since the data are not normally distributed) were statistically significantly different, with a *p*-value of 0.01395 (Mann-Whitney *U*-test, since the data are not normally distributed), whereas the dispersion of the automatically processed data was smaller. Since liver tissue steatosis is a diffuse disease that manifests equally throughout the liver tissue, a decrease in dispersion during processing indicates an increase in the constancy of finding objects with similar characteristics, and may also be the result of a significant increase in the number of objects processed [8].

Fibrosis data with automatic processing have the same dispersion as with manual processing, with a *p*-value of 0.5112. Since in fibrosis, liver tissue is heterogeneous and characterized by the presence of fibrous septa, areas of necrosis and pathological regeneration nodes, stable results are unlikely due to the presence of a large number of different metabolic conditions in hepatocytes, which is also leads to an increase in outliers.

The automatically processed data contains more outliers, which is the result of a decrease in data dispersion. In the graph, to remove outliers, the automatic processing data was filtered by the 5th and 95th percentiles; the data dispersion remained unchanged.

For the automatic data processing option, the patterns of changes at different time points did not differ from those obtained with manual processing, as shown by our statistical tests.

The values of the parameter contributions, i.e. the parameters a_1, a_2 and a_3, differ relatively for automatic and manual calculation by 4.628 ± 3.474%, which is an insignificant difference. The difference in absolute values is due to the difference in the approximation procedure between the SPCImage and the approximation process based on the exponentially modified Gaussian function, which constantly selects components of greater length. The difference in absolute values does not affect the results of analysis due to equivalently changes in contributions between different metabolic statuses and their overall equality.

To assess the compliance of the automatic and manual processing options, a test of the compliance of the mutual distribution of various points of the regeneration process against the background of pathology was carried out. All variants of metabolic states were compared with each other using the Dunn test with Benjamini-Hochberg multiple comparison correction, since the data distribution was statistically significantly different from normal. During the comparison, a matrix was obtained, which indicated the differences between the variants of metabolic states or their absence. During such a comparison for the automatic version of curve analysis and when comparing the results with the manual processing option, error matrices were obtained on the basis of which the precision, recall and F_1 metrics were calculated.

It was shown that for the variant of steatosis pathology development, precision is 0.802, recall is 0.975, F_1 is 0.880, and for the variant of cirrhosis development, precision is 0.731, recall is 0.895, F_1 is 0.805.

The results of the analyses are presented in Fig. 4, Table SI and Table SII.

4 Discussion

Neural networks are currently widely used to facilitate, accelerate, and automate the processing of large volumes of data, including for the analysis of FLIM images.

One example of a CNN-based tool for tissue segmentation is U-SegNet, a full convolutional neural network that has been used to segment brain tissue in MRI images. U-SegNet is a hybrid of two widely used deep learning segmentation architectures, U-Net and SegNet, and has been shown to outperform traditional (manual) brain tissue segmentation methods [3].

Another example is GNN-SEG, a graph-based neural network method also used for brain tissue segmentation; this approach uses to capture the spatial relationships between different brain regions [9].

In addition, a deep learning approach has been proposed for liver and tumor segmentation in CT images using ResUNet [4, 10, 11].

There is a CNN for wound segmentation, which has achieved high accuracy and efficiency, and is applicable to the segmentation of four different types of wound [12].

A neural network model has also been developed to classify stem cells of mesenchymal origin, based on their biomechanical properties [13].

A deep 3D neural network has also been applied to segment brain structures. It used self-monitoring modules to analyze 3D MRI images [14, 15]. The manual segmentation of such magnetic resonance images relies on the use of a highly trained operator to isolate different types of brain structure. The use of neural networks helps automate this process and increases the accuracy and efficiency of segmentation of the brain structures. Applying segmentation to neonatal brain tissue has also been explored for this task [16].

Applicable to FLIM microscopy, research [2] demonstrated the use of a denoising convolutional network to improve the signal-noise ratio (SNR) of the FLIM technique, based on a fast acquisition FLIM system that processes analog signals with large SNRs obtained with the use of highly-efficient pulse modulation.

In addition, for FLIM analysis, Hu et al. proposed an automatic method for segmenting FLIM cell images using multi-resolution community detection (MCD); the method is effective for such segmentation [17].

Another study has demonstrated machine learning methods for the label-free detection of microglia, based on FLIM [15]. The study showed that machine learning methods can be used to better interpret endogenous fluorescent cellular signals in order to characterize microglia, and that this approach can also be extended to other cell types.

In this work, we used the U-Net++ convolutional neural network, which is capable of determining the boundaries of objects with high accuracy. This method has previously shown the value of such accuracy in segmenting medical images of various origins: CT, MRI, microscopy [18].

Our work has demonstrated the high efficiency of applying deep learning methods to segmenting FLIM images; it being shown that automatic image processing not only preserves the characteristics of manual processing in terms of quality, but even surpasses it in coverage of the studied material and in the stability of the results. Similar results have been observed in other studies [19]. In this regard, the use of automatic methods

for analyzing FLIM images is therefore a suitable solution for processing large volumes of data and for express studies of individual samples.

In addition to the possibility of rapid assessment of the liver condition [6, 7, 20], the FLIM method has also proven effective for determining the boundaries of tumor resection [21] and for evaluating the effectiveness of stem cell differentiation in different directions [22, 23]. The algorithm we have developed, in turn, makes it possible to simplify, accelerate and unify the process of processing FLIM data at the cellular level with high spatial and temporal resolution, eliminating the human factor. In particular, the processing time was reduced from 5−15 min to 5−15 s. In the future, software will be developed to improve the usability of the algorithm and create a universal effective tool for a range of applications both in laboratory research and in the clinic.

Using CNNs to analyze medical data has several advantages. First, they can facilitate, speed up, and automate the processing of large volumes of such data, which can be time-consuming and error-prone if done manually. Second, they can improve the accuracy and consistency of medical diagnoses because of their ability to learn from large data sets and generalize these in a way that can be applied to new cases. Third, they can reduce the workload of healthcare professionals, allowing them to focus on more complex tasks that require human expertise [24].

5 Conclusion

FLIM microscopy is widely used to study metabolic changes at the cellular and subcellular levels of various cells and tissues in various physiological and pathological conditions. In this regard, the development of new methods for automating FLIM image processing is an important aspect of the development of diagnostic methods.

A promising direction for solving this problem is the use of neural networks for automatic segmentation of objects of interest on FLIM images and their subsequent analysis.

In this work, we show that the application of neural networks to the task of analyzing metabolic changes in liver tissue during regeneration with pathology corresponds to the quality of the results processed manually. The automated algorithm makes it possible to speed up, standardize and unify the analysis. Although the obtained results look promising, the methods of machine learning and artificial intelligence have their limitations, primarily related to the human factor. The results obtained by the neural network contain artifacts embedded in the learning process, which can only be eliminated by increasing the training sample and introducing a strict data preprocessing protocol. At the same time, the speed of obtaining results, although significantly higher than with manual processing, does not include the time spent on training the neural network and preprocessing the data. In turn, the results of the approximator require fine-tuning.

The obtained results allow us to perform an analysis of metabolic activity, tested, at the moment, only on the model of liver regeneration against the background of pathology, which will allow, in the future, to develop software based on the developed algorithm to create a tool for researches and clinic.

Funding

The work was supported by the Russian Science Foundation Grant №23-15-00421 (metabolic imaging and FLIM analysis), the Russian Science Foundation Grant №24-75-10007 (development of automatized segmentation approach).

Disclosures

The authors declare no conflicts of interest.

Data Availability

Data underlying the results presented in this paper are not publicly available at this time but may be obtained from the authors upon reasonable request.

References

1. W. Becker, “Fluorescence lifetime imaging – techniques and applications,” Journal of Microscopy 247(2), 119–136 (2012).
2. V. Mannam, Y. Zhang, X. Yuan, T. Hato, P. C. Dagher, E. L. Nichols, C. J. Smith, K. W. Dunn, and S. Howard, “Convolutional neural network denoising in fluorescence lifetime imaging microscopy (FLIM),” in Multiphoton Microscopy in the Biomedical Sciences XXI, A. Periasamy, P. T. So, K. König (Eds.), SPIE Proceedings 11648, 116481C (2021).
3. P. Kumar, P. Nagar, C. Arora, and A. Gupta, “U-Segnet: Fully convolutional neural network based automated brain tissue segmentation tool,” 25th IEEE International Conference on Image Processing (ICIP) (IEEE, 2018), 3503–3507 (2018).
4. F. Ouhmich, V. Agnus, V. Noblet, F. Heitz, and P. Pessaux, “Liver tissue segmentation in multiphase CT scans using cascaded convolutional neural networks,” International Journal of Computer Assisted Radiology and Surgery 14(8), 1275–1284 (2019).
5. E. A. Shirshin, M. V. Shirmanova, A. V. Gayer, M. M. Lukina, E. E. Nikonova, B. P. Yakimov, G. S. Budylin, V. V. Dudenkova, N. I. Ignatova, D. V. Komarov, V. V. Yakovlev, W. Becker, E. V. Zagaynova, V. I. Shcheslavskiy, and M. O. Scully, “Label-free sensing of cells with fluorescence lifetime imaging: The quest for metabolic

heterogeneity," Proceedings of the National Academy of Sciences of the United States of America 119(9), e2118241119 (2022).
6. S. Rodimova, N. Bobrov, A. Mozherov, V. Elagin, M. Karabut, I. Shchechkin, D. Kozlov, D. Krylov, A. Gavrina, V. Zagainov, E. Zagaynova, and D. Kuznetsova, "Optical biomedical imaging reveals criteria for violated liver regenerative potential," Cells 12(3), 479 (2023).
7. S. Rodimova, D. Kuznetsova, N. Bobrov, V. Elagin, V. Shcheslavskiy, V. Zagainov, and E. Zagaynova, "Mapping metabolism of liver tissue using two-photon FLIM," Biomedical Optics Express 11(8), 4458 (2020).
8. F. Nassir, R. S. Rector, G. M. Hammoud, and J. A. Ibdah, "Pathogenesis and prevention of hepatic steatosis," Gastroenterlogy and Hepatology 11, 167–175 (2015).
9. C. Wu, Z. Feng, H. Zhang, and H. Yan, "Graph neural network and superpixel based brain tissue segmentation," Proceedings of International Joint Conference on Neural Networks (IJCNN) (2022).
10. H. Rahman, T. F. N. Bukht, A. Imran, J. Tariq, S. Tu, and A. Alzahrani, "A deep learning approach for liver and tumor segmentation in CT images using ResUNet," Bioengineering 9(8), 368 (2022).
11. H. Zhang, K. Luo, R. Deng, S. Li, and S. Duan, "Deep learning-based CT imaging for the diagnosis of liver tumor," Computational Intelligence and Neuroscience 2022, 3045370 (2022).
12. D. Ramachandram, J. L. Ramirez-GarciaLuna, R. D. J. Fraser, M. A. Martínez-Jiménez, J. E. Arriaga-Caballero, and J. Allport, "Fully automated wound tissue segmentation using deep learning on mobile devices: Cohort study," Journal of Medical Internet Research Mhealth Uhealth 10(4), e36977 (2022).
13. E. M. Darling, F. Guilak, "A neural network model for cell classification based on single-cell biomechanical properties," Tissue Engineering Part A 14(9), 1507–1515 (2008).
14. C. Laiton-Bonadiez, G. Sanchez-Torres, and J. Branch-Bedoya, "Deep 3D neural network for brain structures segmentation using self-attention modules in MRI images," Sensors 22(7), 2559 (2022).
15. M. A. K. Sagar, K. P. Cheng, J. N. Ouellette, J. C. Williams, J. J. Watters, and K. W. Eliceiri, "Machine learning methods for fluorescence lifetime imaging (FLIM) based label-free detection of microglia," Frontiers in Neuroscience 14, 931 (2020).
16. Y. Ding, R. Acosta, V. Enguix, S. Suffren, J. Ortmann, D. Luck, J. Dolz, and G. A. Lodygensky, "Using deep convolutional neural networks for neonatal brain image segmentation," Frontiers in Neuroscience 14, 207 (2020).
17. D. Hu, P. Sarder, P. Ronhovde, S. Orthaus, S. Achilefu, and Z. Nussinov, "Automatic segmentation of fluorescence lifetime microscopy images of cells using multiresolution community detection—a first study," Journal of Microscopy 253(1), 54–64 (2014).
18. Z. Zhou, M. M. Rahman Siddiquee, N. Tajbakhsh, and J. Liang, "UNet++: A nested U-Net architecture for medical image segmentation," in Deep Learning in Medical Image Analysis and Multimodal Learning for Clinical Decision Support 11045, 3–11 (2018).
19. M. T. Duong, J. D. Rudie, J. Wang, L. Xie, S. Mohan, J. C. Gee, and A. M. Rauschecker, "Convolutional neural network for automated FLAIR lesion segmentation on clinical brain MR imaging," American Journal of Neuroradiology 40(8), 1282–1290 (2019).
20. E. V. Potapova, V. V. Shupletsov, V. V. Dremin, E. A. Zherebtsov, A. V. Mamoshin, and A. V. Dunaev, "In Vivo time-resolved fluorescence detection of liver cancer supported by machine learning," Lasers in Surgery and Medicine 56(10), 836–844 (2024).
21. M. V. Shirmanova, V. I. Shcheslavskiy, M. M. Lukina, W. Becker, and E. V. Zagaynova, "Exploring tumor metabolism with time-resolved fluorescence methods: from single cells to a whole tumor," Chapter 3 in Multimodal Optical Diagnostics of Cancer, V. V. Tuchin, J. Popp, and V. Zakharov (Eds.), Springer Cham, 133–155 (2020). eBook ISBN: 978-3-030-44594-2.
22. A. V. Meleshina, V. V. Dudenkova, A. S. Bystrova, D. S. Kuznetsova, M. V. Shirmanova, and E. V. Zagaynova, "Two-photon FLIM of NAD(P)H and FAD in mesenchymal stem cells undergoing either osteogenic or chondrogenic differentiation," Stem Cell Research & Therapy 8(1), 15 (2017).
23. S. A. Rodimova, A. V. Meleshina, E. P. Kalabusheva, E. B. Dashinimaev, D. G. Reunov, H. G. Torgomyan, E. A. Vorotelyak, and E. V. Zagaynova, "Metabolic activity and intracellular pH in induced pluripotent stem cells differentiating in dermal and epidermal directions," Methods and Applications in Fluorescence 7(4), 044002 (2019).
24. N. Shahid, T. Rappon, and W. Berta, "Applications of artificial neural networks in health care organizational decision-making: A scoping review," PLoS ONE 14(2), e0212356 (2019).